

Article

Kinetic Control of Anion Stoichiometry in Hexagonal BaTiO₃

Keisuke Kageyama¹, Yang Yang¹, Toki Kageyama¹, Kantaro Murayama¹, Kazuki Shitara², Takashi Saito^{3,4,5}, Hiroki Ubukata¹, Cédric Tassel¹, Akihide Kuwabara² and Hiroshi Kageyama^{1,*} 

¹ Department of Energy and Hydrocarbon Chemistry, Graduate School of Engineering, Kyoto University, Nishikyo-ku, Kyoto 615-8510, Japan; kageyama.keisuke.6n@kyoto-u.ac.jp (K.K.); yang.yang.76p@st.kyoto-u.ac.jp (Y.Y.); toki.k.0507@gmail.com (T.K.); murayama.kantaro.43n@st.kyoto-u.ac.jp (K.M.); ubukata.hiroki.38m@st.kyoto-u.ac.jp (H.U.); cedric@scl.kyoto-u.ac.jp (C.T.)

² Nanostructures Research Laboratory, Japan Fine Ceramics Center, 2-4-1 Mustuno, Atsuta-ku, Nagoya 456-8587, Japan; kazuki_shitara@jfcc.or.jp (K.S.); kuwabara@jfcc.or.jp (A.K.)

³ Institute of Materials Structure Science, High Energy Accelerator Research Organization (KEK), Tokai, Tsukuba 319-1106, Japan; takashi.saito@kek.jp

⁴ Materials and Life Science Division, J-PARC Center, Tokai, Tsukuba 319-1195, Japan

⁵ School of High Energy Accelerator Science, The Graduate University for Advanced Studies (SOKENDAI), Tokai, Tsukuba 319-1195, Japan

* Correspondence: kage@scl.kyoto-u.ac.jp

Abstract: The cubic oxyhydride perovskite BaTiO_{3-x}H_x, where the well-known ferroelectric oxide BaTiO₃ is partially hydridized, exhibits a variety of functions such as being a catalyst and precursor for the synthesis of mixed-anion compounds by utilizing the labile nature of hydride anions. In this study, we present a hexagonal version, BaTi(O_{3-x}H_x) ($x < 0.6$) with the 6H-type structure, synthesized by a topochemical reaction using hydride reduction, unlike reported hexagonal oxyhydrides obtained under high pressure. The conversion of cubic BaTiO₃ (150 nm) to the hexagonal phase by heat treatment at low temperature (950~1025 °C) using a Mg getter allows the introduction of large oxygen defects (BaTiO_{3-x}; $x = 0.28$) while preventing the crystal growth of hexagonal BaTiO₃, which has been accessible at high temperatures of ~1500 °C, contributing to the increase of the hydrogen content. Hydride anions in 6H-BaTiO_{3-x}H_x preferentially occupy face-sharing sites, as do other oxyhydrides.

Keywords: oxyhydride; BaTiO₃; hexagonal; crystal structure



Citation: Kageyama, K.; Yang, Y.; Kageyama, T.; Murayama, K.; Shitara, K.; Saito, T.; Ubukata, H.; Tassel, C.; Kuwabara, A.; Kageyama, H. Kinetic Control of Anion Stoichiometry in Hexagonal BaTiO₃. *Inorganics* **2022**, *10*, 73. <https://doi.org/10.3390/inorganics10060073>

Academic Editors:

Richard Dronskowski, Duncan

H. Gregory, Wolfgang Linert,

Vladimir Arion, Claudio Pettinari

and Torben R. Jensen

Received: 27 April 2022

Accepted: 23 May 2022

Published: 27 May 2022

Publisher's Note: MDPI stays neutral with regard to jurisdictional claims in published maps and institutional affiliations.



Copyright: © 2022 by the authors. Licensee MDPI, Basel, Switzerland. This article is an open access article distributed under the terms and conditions of the Creative Commons Attribution (CC BY) license (<https://creativecommons.org/licenses/by/4.0/>).

1. Introduction

Mixed-anion compounds have been attracting attention as a new class of materials that exhibit novel functions such as high-temperature superconductivity and photocatalysis [1]. Oxyhydrides with the perovskite structure (Figure 1a) and its layered analogues have made remarkable progress in recent years. These include Sr_{n+1}V_nO_{2n+1}H_n showing insulator–metal transition under pressure, SrCrO₂H and LaSrCoO₃H_{0.7} with a high magnetic ordering temperature, and Sr_{n+1}V_nO_{2n+1}H_n ($n = 1$ and $n \rightarrow \infty$), SrCrO₂H, LaSrCoO₃H_{0.7} along with Ba_{2-δ}H_{3-2δ}X (X = Cl, Br, and I) exhibiting hydride (H⁻) anion conductivity [2–5]. A partial hydridization of the well-known ferroelectric oxide BaTiO₃ results in an ammonia synthesis catalyst BaTiO_{3-x}H_x, which is unprecedented given the strong Ti–N bonding. BaTiO_{3-x}H_x is also a stable catalyst for CO₂ hydrogenation despite the generation of water [6–9]. Epitaxial thin film study shows that ATiO_{3-x}H_x (A = Ba, Sr, Ca) is metallic, with a high conductivity of 10²–10⁴ S/cm.

Due to the significant difference in the character of oxides and hydrides, oxyhydrides cannot be synthesized by conventional high-temperature solid-state reactions, with a few exceptions [10]. Some of the perovskite-related oxyhydrides such as LaSrCoO₃H_{0.7}, BaTiO_{3-x}H_x, and SrVO₂H are synthesized by low-temperature topochemical reactions using metal hydrides in vacuo [5,7,11]. An alternate approach is high-pressure synthesis,

which can prevent the release of H₂ from volatile hydrides, yielding, e.g., LaSrMnO_{3.3}H_{0.7} and BaScO₂H [12,13].

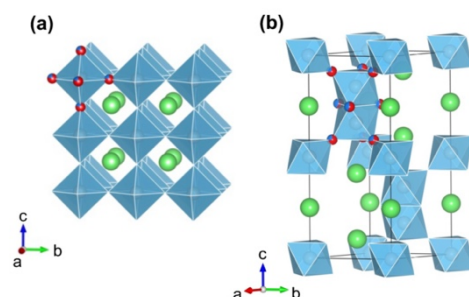


Figure 1. Comparison of the crystal structures of (a) 3C-BaTiO₃ and (b) 6H-BaTiO₃. The green, gray, red, and blue balls represent Ba, Ti, O, and H atoms, respectively.

In contrast to the cubic perovskite (3C-BaTiO₃) with only corner-sharing octahedra, hexagonal perovskite oxyhydrides BaVO_{3-x}H_x and BaCrO₂H with the 6H structure (space group P6₃/mmc), composed of alternating face- and corner-sharing octahedral layers (Figure 1b), have been recently obtained by high-pressure synthesis. BaCrO₂H is a magnetic insulator [14,15]. The preferential occupation of the hydride anion at the face-sharing (6h) crystallographic site enhances the magnetic interaction and provides a high magnetic transition temperature [3]. BaVO_{3-x}H_x also has the hydride anions preferentially occupied at the face-sharing sites, but unlike BaCrO₂H it is a Pauli-paramagnetic metal, with the variable hydride content depending on the synthesis conditions [14].

In this paper, we first show that the oxygen content of the hexagonal perovskite 6H-BaTiO₃ can be tuned widely. We used Mg metal as an oxygen getter to convert the cubic BaTiO₃ to the hexagonal one, 6H-BaTiO_{3-x}, with the maximum content of $x = 0.28$. A subsequent low-temperature topochemical reduction with CaH₂ introduces hydride anions into the hexagonal perovskite lattice, yielding 6H-BaTiO_{3-x}H_x, with the tunable hydride content ($0 \leq x \leq 0.45$) by changing the reducing conditions. The structural characterization has revealed the preferential occupation of the oxygen vacancies in 6H-BaTiO_{3-x} and the hydride anions in 6H-BaTiO_{3-x}H_x, at the face-sharing site, which is supported by DFT calculations. The initial introduction of oxygen defects, along with the small grain size, are critically important for the hydride ion content of the final product, indicating the importance of the kinetic control to obtain the desired structures and compositions.

2. Experimental Section

We carried out hydride reductions using two types of hexagonal perovskite BaTiO₃. One is 6H-BaTiO₃ (BTO-L) with large particles of ~100 μm, provided by Murata Manufacturing Co. BTO-L was fabricated by H₂ reduction of BaTiO₃ (Sakai Chemicals, BT-03) at 1450 °C for 1 h. A mixture of BTO-L and CaH₂ (99.7%, Aldrich) at a molar ratio of 10:1 was vacuum-sealed in a Pyrex tube and heat-treated at 520 °C for 72 h (L-1), 120 h (L-2), and 168 h (L-3), respectively. The large particle size of BTO-L is consistent with the fact that the synthesis of 6H-BaTiO₃ requires calcination at high temperatures (1400–1500 °C) in a reducing atmosphere, but this is not suitable for anion (H⁻/O²⁻) exchange reactions, as will be shown later [11,16].

In order to obtain 6H-BaTiO₃ with a smaller grain size to promote the anion exchange, we have developed a new method to convert cubic BaTiO₃ into the hexagonal phase (BTO-S) by treating it with Mg at relatively low temperatures. First, BaTiO₃ (~100 nm), provided by Sakai Chemicals (BT-01), was pelletized, and the pellet was sandwiched between pellets of equal weight mixtures of cubic BaTiO₃ and Mg (>99.7%, Fujifilm Wako Chemicals Corporation) as a sacrificial reagent, sealed in a quartz tube under vacuum, and heat-treated at 950–1025 °C for 10 h. This procedure was repeated until the starting cubic BaTiO₃ phase disappeared, as observed by XRD analysis. Next, the obtained 6H-BaTiO₃

was washed with a 1:3 mixture of acetic acid and methanol at 60 °C for more than 10 h to remove MgO. Then, the BTO-S powder was mixed with 10 molar ratio CaH₂ in an immersion mortar, vacuum-sealed in a Pyrex tube, and heat-treated at 450–520 °C for 120 h to obtain hydride samples. The conditions for the samples synthesized in this study are shown in Table S1.

The crystal structures of the samples were examined by laboratory X-ray diffraction (XRD) measurements using a Smart Lab diffractometer (Rigaku) with Cu K α radiation. High-resolution powder synchrotron XRD (SXR) experiments were performed at room temperature (RT) using the BL02B2 beamline of the Japan Synchrotron Radiation Research Institute (JASRI). Incident beams from a bending magnet were monochromatized either to $\lambda = 0.419839(1)$, $0.42015(1)$, or $0.42053(1)$ Å. Powder samples were loaded into Pyrex capillaries with an inner diameter of 0.3 mm. The sealed capillary was rotated during the measurements to reduce the effect of preferred orientation of crystallites. Neutron powder diffraction (NPD) data were collected at RT using the BL09 SPICA beamline at the Japan Proton Accelerator Research Complex (J-PARC). The collected SXR and NPD patterns were analyzed by the Rietveld method using RIETAN-FP program for SXR data and Z-Rietveld program for NPD data [17–20].

The release of hydrogen was monitored upon heating using a Bruker MS9610 quadrupole mass spectrometer (QMS). The sample was heated up to 800 °C under flowing Ar gas at a 300 mL/min rate. Thermogravimetric (TG) measurements were performed with a Netzsch TG-DTA 2000SE up to 800 °C under flowing O₂ gas at 300 mL/min rate. Platinum pans were used to hold both the sample and Al₂O₃ as a reference. A Quantum Design MPMS-XL SQUID magnetometer was used to measure the magnetic susceptibility of the sample with an applied magnetic field of 0.1 T from 2 K to 350 K.

DFT calculations were performed using the projector augmented wave method as implemented in the VASP code [21,22]. An exchange correlation term was treated with the Perdew–Burke–Ernzerhof functional [23]. We considered all possible structures of the symmetrically independent O/H configurations in the hexagonal cell with compositions of Ba₆Ti₆O_{18-n}H_n (where $n = 1, 2, \dots, 6$). For $n = 1$, we introduced one H into the symmetrically independent O site, O1 or O2. Symmetrically nonequivalent configurations for $n = 1$ amount to 2, as shown in Table S2. For $n = 2$, an additional H was placed to the symmetrically independent anion site into these structures. Symmetrically independent sites were searched based on space group using spglib library [24]. This process was repeated 6 times, preparing all the possible symmetrically independent O/H configurations up to $n = 6$. All the symmetrically nonequivalent configurations amount to 1496, shown in Table S2. We constructed 1496 input models, and for each model the total energy was minimized until the energy convergences became less than 10^{-5} eV during self-consistent cycles. Atomic positions and lattice constants were relaxed until the residual atomic forces became less than 0.02 eV Å⁻¹. Correlation effects of 3d orbitals with the effective U potential of 4.49 eV were taken into account within the framework of the GGA+U method [25–27]. The effective plane-wave cutoff energy was set to 550 eV. Integration in reciprocal space was performed with a $5 \times 5 \times 2$ grid. Furthermore, we analyzed the relationship between formation energies and structural parameters using a linear regression method. A database of the formation energies and the structural parameters was constructed from the calculations of 1496 independent configurations.

3. Results and Discussion

Figure 2 shows the XRD patterns of BTO-L and its reduced products. The diffraction pattern of the precursor BTO-L can be indexed with a hexagonal lattice and the cell parameters of $a = 5.726(1)$ Å and $c = 13.970(1)$ Å, in good agreement with the reported values of 6H-BaTiO₃ [28]. After hydride reduction at 520 °C for 72 h, all the peaks shifted to the lower angles, yielding the elongated lattice constants of $a = 5.753(1)$ Å and $c = 14.070(1)$ Å. The lattice expansion is attributed to the partial reduction of Ti⁴⁺ to Ti³⁺ by anion (H⁻/O²⁻) exchange, as observed in the reduction of tetragonal BaTiO₃ to cubic BaTiO_{2.4}H_{0.6} [8].

No impurity phases were observed. The TG measurement of the sample after hydride reduction showed a substantial weight gain (Figure S1a), and the QMS measurement under argon atmosphere showed the hydrogen gas release as observed in other oxyhydrides (Figure S1b), suggesting the successful formation of an oxyhydride [6,8,11,15,28].

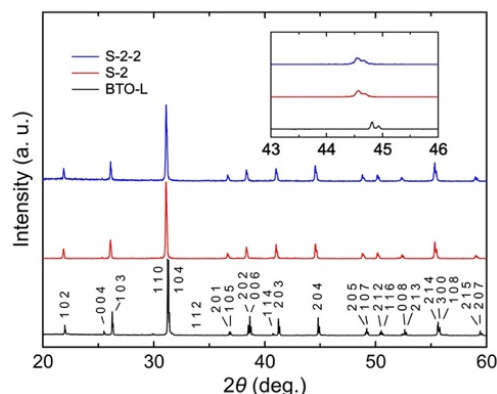


Figure 2. XRD patterns of the polycrystalline 6H-BaTiO_{3-x} and $6\text{H-BaTiO}_{3-x}\text{H}_x$. The S-2 sample was synthesized by the Mg reduction twice at $1000\text{ }^\circ\text{C}$ for 10 h, which was further subject to hydride reduction with CaH_2 at $520\text{ }^\circ\text{C}$ for 120 h to produce S-2-2, in contrast to BTO-L prepared by H_2 reduction at $1450\text{ }^\circ\text{C}$ for 1 h.

The longer reaction time of hydride reduction ($520\text{ }^\circ\text{C}$) with BTO-L (L-1, L-2, L-3) resulted in the larger lattice parameters (Figure S2), similar to the case of cubic perovskite $\text{ATi}(\text{O}_{3-x}\text{H}_x)$ ($A = \text{Ba}, \text{Sr}, \text{Ca}$) [8,29]. The elongation of the c -axis relative to its precursor oxide is more pronounced than that of the in-plane axes (Figure S2), which is also consistent with the trend observed in other hexagonal (6H) perovskite oxyhydrides, $\text{BaV}(\text{O}_{3-x}\text{H}_x)$ and BaCrO_2H , in comparison with corresponding oxides [15,28]. However, several XRD peaks of BTO-L after hydride reduction exhibit shoulders, which could be due to a distribution in hydrogen content caused by the use of large particles, as also observed in cubic perovskite $\text{ATi}(\text{O}_{3-x}\text{H}_x)$ ($A = \text{Ba}, \text{Sr}, \text{Ca}$) [8]. This prevented precise structural and compositional analysis of the oxyhydride phases.

The hexagonal barium titanate is stabilized by introducing oxygen vacancies (x in 6H-BaTiO_{3-x}) with a tendency of the lattice constant increasing with x [30]. As mentioned earlier, this phase is accessible at $1400\text{--}1500\text{ }^\circ\text{C}$ in flowing H_2 , but we hypothesized that further removal of the lattice oxygen would stabilize the hexagonal phase at lower temperatures where particle growth can be suppressed [16]. Figure 2 shows the XRD pattern of sample S-2, obtained by the heat treatment of cubic BaTiO_3 ($\sim 100\text{ nm}$) at $1000\text{ }^\circ\text{C}$ for 10 h ($\times 2$) in a vacuum using Mg as an oxygen getter. All the diffraction peaks were assigned with the hexagonal cell ($\text{P6}_3/\text{mmc}$) structure, indicating the complete conversion from the cubic phase even at low temperatures. The SEM images of BTO-S revealed that the articles grew only slightly ($\sim 250\text{ nm}$) (Figure S3).

The Rietveld analysis of the SXRD data of sample S-2 (6H-BaTiO_{3-x}) was performed using the $\text{P6}_3/\text{mmc}$ model (Figure 3). The occupancy factors (g) for the two oxygen sites are determined to be $g = 0.72(1)$ for the O1 ($6h$) site and $g = 0.995(1)$ for the O2 ($12k$) site. Thus, the O2 site was assumed to be fully occupied (thus giving $6\text{H-BaTiO}_{0.72}$) in the following analysis. The dominant creation of oxygen vacancy at the face-sharing site is consistent with previous studies [30]. By changing the severity of the Mg reduction conditions ($950\text{--}1025\text{ }^\circ\text{C}$ for 10 h), we are able to widely tune the oxygen-vacancy content (Table S1). The lattice parameters as a function of oxygen vacancy content x (6H-BaTiO_{3-x}) are shown in Figure 4, along with those presented by Akimoto [28] and Sinclair [30]. Both the a -axis and the c -axis increase in proportion with oxygen deficiency. SXRD data of 6H-BaTiO_{3-x} prepared under different Mg-reduction conditions of BTO-S were analyzed by Rietveld analysis. The crystallographic parameters and the compositions estimated from

the occupancy of O1 ($6h$) sites are summarized in Table S3, and lattice parameters in terms of oxygen contents are shown in Figure 4, along with those presented by Akimoto et al. and Sinclair et al. [28,30]. Both the in-plane and out-of-plane axes are elongated with increasing oxygen deficiency, which can be understood in terms of the enhanced Coulombic repulsion between Ti2 and Ti2.

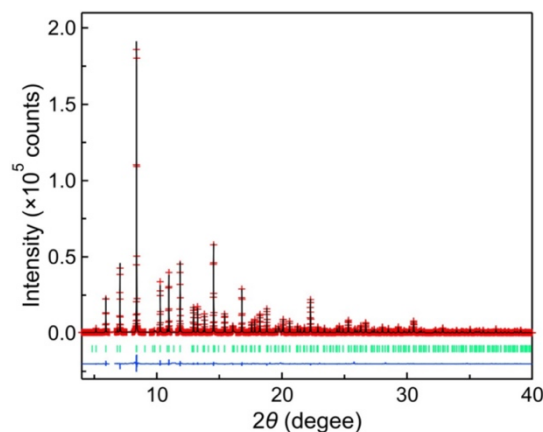


Figure 3. Result of Rietveld refinement of SXR D data for the S-2 sample prepared by reducing twice with Mg at 1000 °C for 10 h with $\lambda = 0.419839(1)$ Å. The red crosses, black line, blue line, and green dashes denote, respectively, the observed, calculated, difference intensities, and Bragg positions.

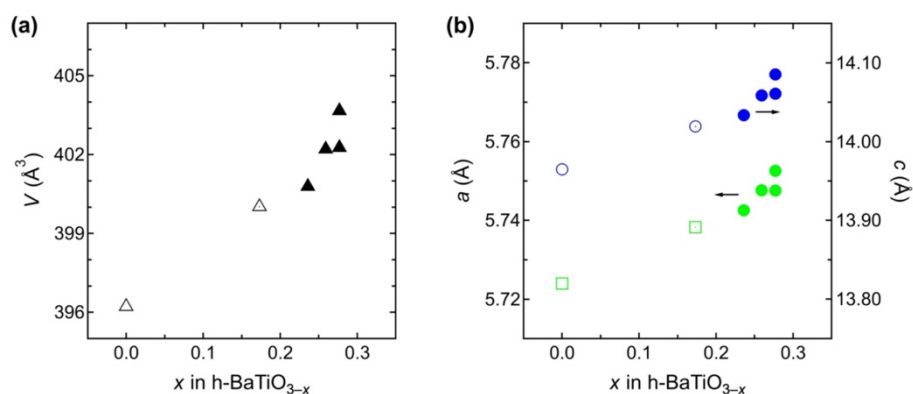


Figure 4. Lattice parameters of (a) V , (b) a , and c as a function of x taken from 6H-BaTiO₃ (after Akimoto [28]), 6H-BaTiO_{2.83} (after Sinclair [30]), and 6H-BaTiO_{3-x} in this work (see Table S3-5). The errors are within the size of the symbols.

When 6H-BaTiO_{2.72} (derived from sample S-2 in Table S3-2) was reacted at 520 °C for 120 h using CaH₂, the XRD peaks shifted to lower angles than those of 6H-BaTiO₃ (BTO-L) after the same hydride treatment, and the elongated lattice constants of $a = 5.7664(1)$ Å and $c = 14.0713(1)$ Å were obtained as shown in Table S4-5. The SXR D data of 6H-BaTiO_{2.72} after hydride reduction (sample S-2-2) were analyzed by the Rietveld analysis assuming an oxygen-deficient 6H-BaTiO_{3-x} (space group P6₃/mmc), without considering hydride anions (Figure 5a and Table S4-5), which yielded the occupancy factor of O2 of 0.99(1); thus, we fixed it as unity for later refinements. On the other hand, the occupancy factor at the O1 site was determined as 0.55(1), giving $x = 0.45(1)$. The tendency of the hydride anion to occupy the face-sharing site is similar to that of 6H-BaV(O_{3-x}H_x) and 6H-BaCrO₂H [15,16].

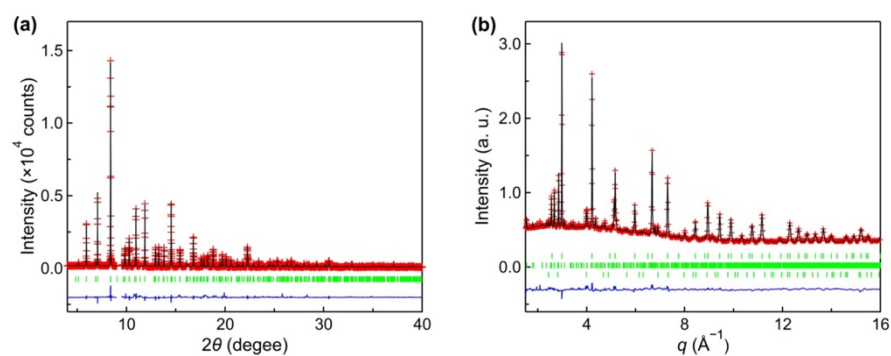


Figure 5. Rietveld analysis against (a) SXR D and (b) ND pattern of S-2-2 synthesized by Mg reduction twice at 1000 °C for 10 h and hydrogenated with CaH₂ at 520 °C for 120 h with $\lambda = 0.420526(1)$ Å (SXR D). The red crosses, black line, blue line, and green dashes denote, respectively, the observed, calculated, difference intensities, and Bragg positions.

The Rietveld analysis was carried out using the time-of-flight neutron diffraction data of the same specimen (Figure 5b and Table S4-5; sample S-2-2). According to the synchrotron result, the occupancy of the O2 site was set to unity, and anion vacancies at the O1 were not considered. The occupancy factors of oxide and hydride anions at the O1 site were obtained as 0.54(2) and 0.46(2), respectively, yielding the composition of BaTiO_{2.54}H_{0.46}. The result of QMS in Ar gas flow, shown in Figure 6, supports the inclusion of a large amount of hydride anions in the hexagonal perovskite structure. The magnetic susceptibility of S-2-2 (Figure 7) is nearly temperature-independent, a typical behavior for paramagnetic metal, and no difference is seen between field cooling (FC) and zero field cooling (ZFC) processes. These facts indicate that the reaction proceeded further than in the case of the BTO-L case with the replacement of O²⁻ and the vacancies with H⁻ [6,11,31].

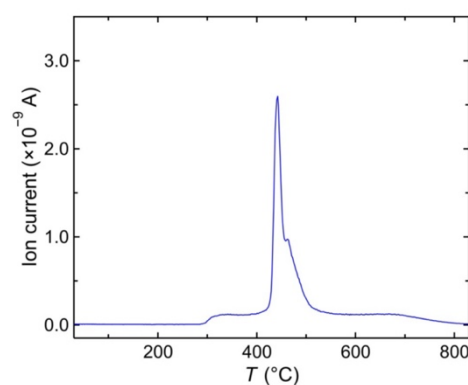


Figure 6. Quadrupole mass spectrometry of H₂ during heating of the S-2-2 which is prepared by twice heat treatment at 1000 °C for 10 h and subsequent hydrogenation with CaH₂ at 520 °C for 120 h.

As in the case of BTO-L, by changing the reaction temperature and duration for hydride reduction of BTO-S, the amount of hydride can be varied. Note that the hydride topochemical reaction above 560 °C for BTO-L and those above 500 °C for BTO-S resulted in the appearance of TiH₂ impurity. We additionally found that the amount of oxygen vacancy in the parent oxide 6H-BaTiO_{3-x} affects the insertion efficiency of hydride anions; the higher/longer the reaction temperature/time of the CaH₂ reduction, the higher the amount of H⁻ is. Samples of S-1-1~S-1-3, S-2-1, S-2-2, S-3-1, and S-4-1 (Table S4) show varied H⁻ anion content, depending on CaH₂ reduction conditions (Figure S4). With increasing CaH₂-reduction temperature, H⁻ anion content increases. The H⁻ contents are estimated from the occupancy (g) of oxygen assuming ‘oxygen deficiencies’ are filled fully with H⁻ anions. As shown in Table S3-5 (sample S-2-2), the occupancy of H⁻ in O1 site from the ND analysis is 0.46(2), in good agreement with the value of 0.45(1)

obtained from SXRD analysis, supporting the above assumption. The importance of the initial inclusion of anion deficiency for anion exchange reactions has been underlined in the topochemical synthesis of oxyhydrides of $\text{Sr}(\text{Ti}_{1-x}\text{Sc}_x)(\text{O},\text{H})_3$ and $\text{CaV}(\text{O}_{3-x}\text{H}_x)$ and oxynitrides of EuTiO_2N [31–33].

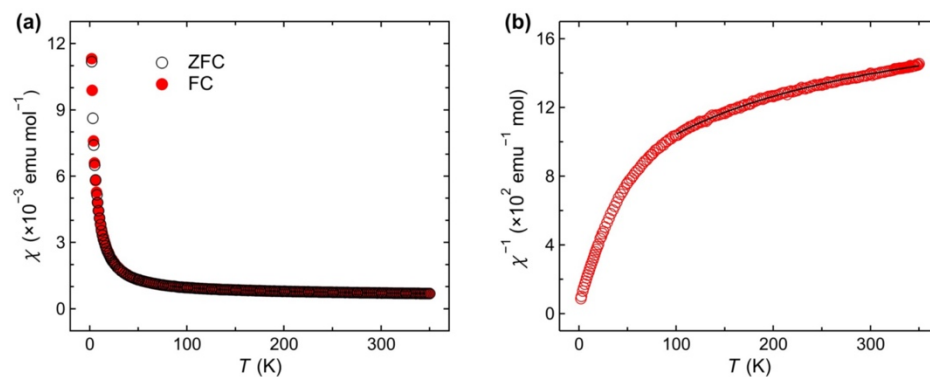


Figure 7. (a) Magnetic susceptibility as a function of temperature for S-2-2 collected at 0.1 T in field cooling (FC) and zero field cooling (ZFC) processes. (b) Curie fitting following Curie–Weiss law ($\chi(T) = C/(T - \theta) + \chi_0$) in the temperature range $100 \text{ K} < T < 350 \text{ K}$ of FC data, yielding values of $C = 7.2(2) \times 10^{-2} \text{ emu/K mol}$, $\chi_0 = 5.20(4) \times 10^{-4} \text{ emu/mol}$, $\theta_w = -65(4) \text{ K}$, where C , θ , and χ_0 stand for the Curie constant, Weiss temperature, and a constant.

As shown in Figure 8, the a - and c -axes and volume tend to increase with the H^- content. Interestingly, this trend is suppressed beyond a hydride content of $x = 0.4$. The atomic distance between Ti2 and Ti2 nearest neighbors obtained from Rietveld analysis (see Figure 9a,b), i.e., titanium cations in face-sharing octahedra, increases in response to the increase in oxygen deficiency in 6H-BaTiO_{3-x} (Figure 9c), but in $6\text{H-BaTiO}_{3-x}\text{H}_x$ the Ti2–Ti2 interatomic distance decreases in contrast to the Ba1–O1 distance (Figure 9d). In $6\text{H-BaCrO}_2\text{H}$, the Cr–Cr distance at the face-sharing site is greatly extended compared to BaCrO_3 , which is discussed together with enhanced magnetic interactions in terms of the highly polarized H ions [15]. A simple explanation for this behavior of our compounds is not possible at present, but various factors such as kinetic factors and local distortions are likely to be involved. We believe that further studies, including local structure analysis and in-depth theoretical studies, are needed in the future.

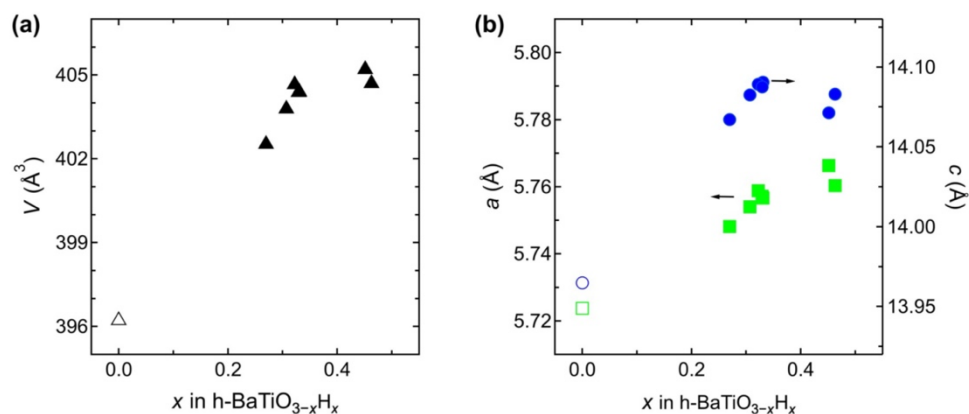


Figure 8. Cell parameters of (a) V , (b) a , and c as a function of x in $6\text{H-BaTiO}_{3-x}\text{H}_x$ (see Table S4–8). The errors are within the size of the symbols. The values for $x = 0$ (open symbols) are taken after Akimoto [28].

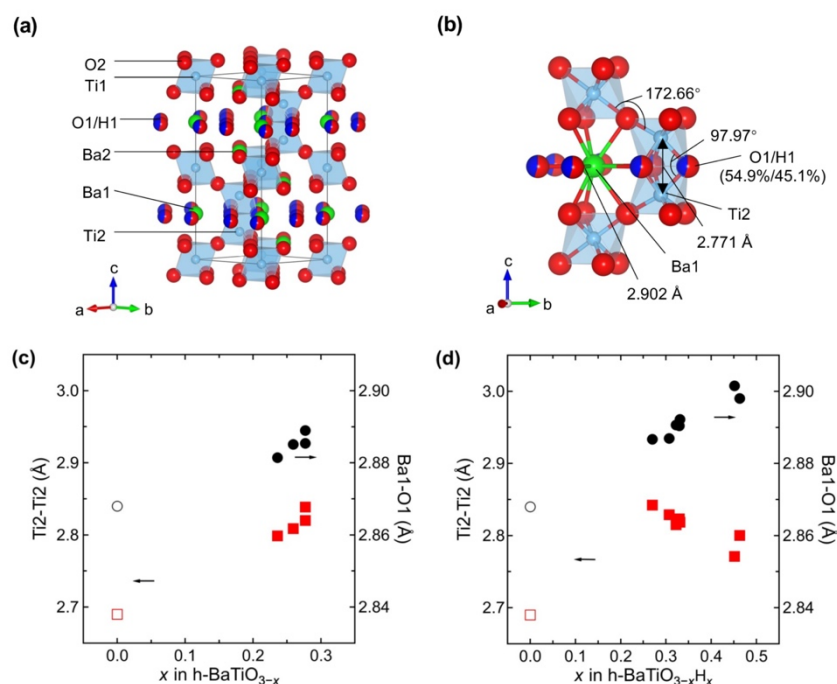


Figure 9. (a) Crystal structure of $6\text{H-BaTiO}_{3-x}\text{H}_x$, where green, white, red, and blue spheres represent Ba, Ti, O, and H atoms, respectively. (b) Local geometry around Ba and Ti cations for $\text{BaTiO}_{2.55}\text{H}_{0.45}$. Interatomic distances of Ti2–Ti2 and Ba1–O1 as a function of oxygen deficiency x for (c) 6H-BaTiO_{3-x} and hydride content for (d) $6\text{H-BaTiO}_{3-x}\text{H}_x$. The values of $x = 0$ (after Akimoto [28]) are shown in open symbols for comparison. The errors are within the size of the symbols.

DFT calculations were also performed for the transition metal Ti (d^1) to examine the site preference of the hydride anion in $6\text{H-BaTiO}_{3-x}\text{H}_x$. We have calculated the energies of all possible structures of the independent 1496 coordination in $\text{Ba}_6\text{Ti}_6\text{O}_{18-n}\text{H}_n$ ($n = 1, 2, \dots, 6$; Table S2) to know which site the hydrogen ion is more likely to occupy. The most stable configurations obtained for each n are shown in Figure S5, showing that when n is one to five, hydride anions preferentially occupy the face-sharing site. When n is six, hydride anions start to occupy the corner-sharing site, but the preference of *cis*- and *trans*- seems to be weaker than that of $\text{BaVO}_{3-x}\text{H}_x$ [14] (see supporting information, Figures S6 and S7 and Table S2). Furthermore, theoretically, the H^- anion in $\text{BaTiO}_{3-x}\text{H}_x$ has a stronger tendency to occupy the 6h site (vs. the 12k site) than that of V in $\text{BaVO}_{3-x}\text{H}_x$, in particular for $x < 0.33$ (Table S4-5). This is consistent with the experimental observation in $\text{BaVO}_{2.7}\text{H}_{0.3}$ [14].

During the final preparation stage of this manuscript, we become aware of the report of $6\text{H-BaTiO}_{2.01}\text{H}_{0.96}$, which was prepared from the direct reaction of BaH_2 and TiO_2 [34]. The material catalyzes the hydrogenation of the unsaturated C–C bonds when used as a support of Pd nanoparticles.

4. Conclusions

The hexagonal form of BaTiO_{3-x} in a wide range of oxygen deficiencies, with the maximum content of $x = 0.28$, was synthesized from cubic BaTiO_3 under strong reducing condition using Mg as an oxygen getter. In 6H-BaTiO_{3-x} , oxygen vacancies are exclusively introduced into the face-sharing Ti-centered octahedral site O1. Low-temperature CaH_2 reduction of the obtained 6H-BaTiO_{3-x} yielded oxyhydride $6\text{H-BaTiO}_{3-x}\text{H}_x$ with H^- ions occupying only at the face-sharing site O1, which is supported by DFT calculations. The initial introduction of oxygen defects, along with small grain size, is critically important for the hydride ion content of the final product, indicating the importance of the kinetic control to obtain the desired structures and compositions.

Supplementary Materials: The following supporting information can be downloaded at: <https://www.mdpi.com/article/10.3390/inorganics10060073/s1>, Figure S1: Results of (a) thermogravimetric analysis, which was performed in oxygen flow at a rate of 300 mL/min; (b) quadruple mass spectrometry of H₂; Figure S2: The relationship between lattice parameters (a) c, (b) a, and reaction time for the 6H-BaTiO_{3-x}H_x reduced by H₂ at 1450 °C for 1 h and hydrogenated with CaH₂ at 520 °C; Figure S3: SEM images of 6H BaTiO_{3-x}. (a) Specimen prepared by H₂ reduction at 1450 °C for 1 h (BTO-L); (b) specimen prepared by Mg reduction twice at 1000 °C for 10 h (BTO-S); Figure S4: Variation of hydrogen content in 6H-BaTiO_{3-x}H_x as a function of hydrogenation temperature by CaH₂ reduction; Figure S5: The (a) 1st, (b) 2nd, and (c) 5th most stable structures in 6H-type system for Ba₆Ti₆O₁₆H₂ obtained by the DFT calculations; Figure S6: Relationship between predicted energies from LASSO regression [35] and DFT calculations for Ba₆Ti₆O₁₆H₂; Figure S7: Obtained coefficients from LASSO regression; Table S1: Sample lists. (a) BaTiO₃ (BT03, Sakai) was reduced in H₂ atmosphere and hydrided by CaH₂. (b–e) BaTiO₃ (BT01, Sakai) was prepared by Mg reduction method and hydrided by CaH₂; Table S2: Number of symmetrically independent O/H configurations of a hexagonal unit cell with the composition of Ba₆Ti₆O_{18-n}H_n ($n = 1\sim6$); Table S3: Crystallographic parameters of 6H-BaTiO_{3-x} with varied oxygen deficiencies prepared by Mg reduction; Table S4: Crystallographic data analyzed by the Rietveld analysis against SXRD and the NPD patterns of 6H-BaTiO_{3-x}H_x prepared by Mg reduction in different conditions; Table S5: List of descriptors of structural parameters.

Author Contributions: Conceptualization, H.K.; methodology, T.K. and K.K.; validation, Y.Y. and H.K.; formal analysis, K.K., T.K., K.M., K.S., T.S. and A.K.; investigation, T.K. and K.K.; resources, H.K.; data curation, K.K., T.K., H.K., K.S., T.S. and A.K.; writing—original draft preparation, K.K.; writing—review and editing, H.K., Y.Y., K.S., H.U., C.T. and A.K.; visualization, Y.Y.; supervision, H.K.; project administration, H.K.; funding acquisition, H.K. All authors have read and agreed to the published version of the manuscript.

Funding: This research was funded by CREST grant numbers JPMJCR1421 and JPMJCR20R2; JSPS KAKENHI grant numbers JP16H06438, JP16H06439, JP16H06440, JP16H06441, and JP19H04710; Nanotechnology Platform Program (Molecule and Material Synthesis) (S-20-MS-0015) from the Ministry of Education, Culture, Sports, Science and Technology (MEXT) of Japan; and the Japan Society for the Promotion of Science (JSPS) Core-to-Core Program (JPJSCCA20200004).

Institutional Review Board Statement: Not applicable.

Informed Consent Statement: Not applicable.

Data Availability Statement: Not applicable.

Acknowledgments: The authors are grateful for the financial support from CREST, grant numbers JPMJCR1421 and JPMJCR20R2; JSPS KAKENHI grant numbers JP16H06438, JP16H06439, JP16H06440, JP16H06441, and JP19H04710; Nanotechnology Platform Program (Molecule and Material Synthesis) (S-20-MS-0015) from the Ministry of Education, Culture, Sports, Science and Technology (MEXT) of Japan; and the Japan Society for the Promotion of Science (JSPS) Core-to-Core Program (JPJSCCA20200004); and also grateful for the SXRD experiments performed at SPring-8 with the approval of JASRI and the NPD experiment performed at J-PARC. Y.Y. is grateful for the scholarship from China Scholarship Council (CSC).

Conflicts of Interest: The authors declare no conflict of interest.

References

1. Kageyama, H.; Hayashi, K.; Maeda, K.; Attfield, J.P.; Hiroi, Z.; Rodonelli, J.M.; Poeppelmeier, K.R. Expanding frontiers in materials chemistry and physics with multiple anions. *Nat. Commun.* **2018**, *9*, 772. [[CrossRef](#)]
2. Ochi, M.; Kuroki, K. Effective Interaction for Vanadium Oxyhydrides Sr_{n+1}V_nO_{2n+1}H_n ($n = 1$ and $n \rightarrow \infty$): A Constrained-RPA Study. *Phys. Rev. B Condens. Matter Mater. Phys.* **2019**, *99*, 155143. [[CrossRef](#)]
3. Tassel, C.; Goto, Y.; Kuno, Y.; Hester, J.; Green, M.; Kobayashi, Y.; Kageyama, H. Direct Synthesis of Chromium Perovskite Oxyhydride with a High Magnetic-Transition Temperature. *Angew. Chem. Int. Ed.* **2014**, *53*, 10377–10380. [[CrossRef](#)] [[PubMed](#)]
4. Ubukata, H.; Takeiri, F.; Shitara, K.; Tassel, C.; Saito, T.; Kamiyama, T.; Broux, T.; Kuwabara, A.; Kobayashi, G.; Kageyama, H. Anion Ordering Enables Fast H⁻ Conduction at Low Temperatures. *Sci. Adv.* **2021**, *7*, eabf7883/1-7. [[CrossRef](#)]
5. Hayward, M.A.; Cussen, E.; Claridge, J.; Bieringer, M.; Rosseinsky, M.; Kiely, C.; Blundell, S.; Marshall, I.; Pratt, F. The hydride anion in an extended transition metal oxide array: LaSrCoO₃H_{0.7}. *Science* **2002**, *295*, 1882–1884. [[CrossRef](#)]

6. Devonshire, A.F. CIX. Theory of barium titanate—Part II. *Lond. Edinb. Dublin Philos. Mag. J. Sci.* **1951**, *42*, 1065–1079. [[CrossRef](#)]
7. Kobayashi, Y.; Hernandez, O.J.; Sakaguchi, T.; Yajima, T.; Roisnel, T.; Tsujimoto, Y.; Morita, M.; Noda, Y.; Mogami, Y.; Kitada, A.; et al. An oxyhydride of BaTiO₃ exhibiting hydride exchange and electronic conductivity. *Nat. Mater.* **2012**, *11*, 507–511. [[CrossRef](#)] [[PubMed](#)]
8. Kobayashi, Y.; Tang, Y.; Kageyama, T.; Yamashita, H.; Masuda, N.; Hosokawa, H.; Kageyama, H. Titanium-Based Hydrides as Heterogeneous Catalysts for Ammonia Synthesis. *J. Am. Chem. Soc.* **2017**, *139*, 18240–18246. [[CrossRef](#)] [[PubMed](#)]
9. Tang, T.; Kobayashi, Y.; Tassel, C.; Yamamoto, T.; Kageyama, H. Hydride-Enhanced CO₂ Methanation: Water-Stable BaTiO_{2.4}H_{0.6} as a New Support. *Adv. Energy Mater.* **2018**, *8*, 1800800. [[CrossRef](#)]
10. Widerøe, K.; Fjellvag, H.; Norby, T.; Willy, F.; Rolf, P.; Berg, W. NdHO, a novel oxyhydride. *J. Solid State Chem.* **2011**, *184*, 1890–1894. [[CrossRef](#)]
11. Bang, J.; Matsuishi, S.; Hiraka, H.; Fujisaki, F.; Otomo, T.; Maki, S.; Yamaura, J.; Kumai, R.; Murakami, Y.; Hosono, H. Hydrogen Ordering and New Polymorph of Layered Perovskite Oxyhydrides: Sr₂VO_{4-x}H_x. *J. Am. Chem. Soc.* **2014**, *136*, 7221–7224. [[CrossRef](#)] [[PubMed](#)]
12. Tassel, C.; Goto, Y.; Watabe, D.; Tang, Y.; Lu, H.; Kuno, Y.; Takeiri, F.; Yamamoto, T.; Brown, C.M.; Hester, J.; et al. High-Pressure Synthesis of Manganese Oxyhydride with Partial Anion Order. *Angew. Chem. Int. Ed.* **2016**, *55*, 9667–9670. [[CrossRef](#)] [[PubMed](#)]
13. Goto, Y.; Tassel, C.; Noda, Y.; Hernandez, O.; Pickard, C.J.; Green, M.A.; Sakaebe, H.; Taguchi, N.; Uchimoto, Y.; Kobayashi, Y.; et al. Pressure-Stabilized Cubic Perovskite Oxyhydride BaScO₂H. *Inorg. Chem.* **2017**, *56*, 4840–4845. [[CrossRef](#)] [[PubMed](#)]
14. Yamamoto, T.; Shitara, K.; Kitagawa, S.; Kuwabara, A.; Kuroe, M.; Ishida, K.; Ochi, M.; Kuroki, K.; Fujii, K.; Yashima, M.; et al. Selective Hydride Occupation in BaVO_{3-x}H_x (0.3 ≤ x ≤ 0.8) with Face- and Corner-Shared Octahedra. *Chem. Mater.* **2018**, *30*, 1566–1574. [[CrossRef](#)]
15. Higashi, K.; Ochi, M.; Nambu, Y.; Yamamoto, T.; Murakami, T.; Yamashina, N.; Tassel, C.; Matsumoto, Y.; Takatsu, H.; Brown, M.C.; et al. Enhanced Magnetic Interaction by Face-Shared Hydride Anions in 6H-BaCrO₂H. *Inorg. Chem.* **2021**, *60*, 11957–11963. [[CrossRef](#)]
16. Recnik, A.; Kolar, D. Exaggerated Growth of Hexagonal Barium Titanate under Reducing Sintering conditions. *J. Am. Ceram. Soc.* **1996**, *79*, 1015–1018. [[CrossRef](#)]
17. Izumi, F.; Momma, K. Three-Dimensional Visualization in Powder Diffraction. *Solid State Phenom.* **2007**, *130*, 15. [[CrossRef](#)]
18. Momma, K.; Izumi, F. VESTA 3 for Three-Dimensional Visualization of Crystal, Volumetric and Morphology. *J. Appl. Crystallogr.* **2011**, *44*, 1272–1276. [[CrossRef](#)]
19. Oishi, R.; Yonemura, M.; Nishimaki, Y.; Torii, S.; Hoshikawa, A.; Ishigaki, T.; Morishima, T.; Mori, K.; Kamiyama, T. Rietveld analysis software for J-PARC. *Nucl. Instrum. Methods Phys. Res. Sect. A* **2009**, *600*, 94–96. [[CrossRef](#)]
20. Oishi, R.; Yonemura, M.; Morishima, T.; Hoshikawa, A.; Torii, S.; Ishigaki, T.; Kamiyama, T. Application of matrix decomposition algorithms for singular matrices to the Pawley method in Z-Rietveld. *J. Appl. Crystallogr.* **2012**, *45*, 299–308. [[CrossRef](#)]
21. Kresse, G.; Hafner, J. Ab initio molecular dynamics for liquid metals. *Phys. Rev. B Condens. Matter Mater. Phys.* **1993**, *47*, 558–561. [[CrossRef](#)] [[PubMed](#)]
22. Kresse, G.; Furthmüller, J. Efficient iterative schemes for ab initio total-energy calculations using a plane-wave basis set. *Phys. Rev. B Condens. Matter Mater. Phys.* **1996**, *54*, 11169–11186. [[CrossRef](#)] [[PubMed](#)]
23. Perdew, J.P.; Burke, K.; Ernzerhof, M. Generalized gradient approximation made simple. *Phys. Rev. Lett.* **1996**, *77*, 3865–3868. [[CrossRef](#)] [[PubMed](#)]
24. Togo, A. SPGLIB: A C Library for Finding and Handling Crystal Symmetries. Available online: <https://atztogo.github.io/spglib/> (accessed on 6 December 2017).
25. Wang, L.; Maxisch, T.; Ceder, G. Oxidation energies of transition metal oxides within the GGA U framework. *Phys. Rev. B Condens. Matter Mater. Phys.* **2006**, *73*, 195107. [[CrossRef](#)]
26. Jain, A.; Hautier, G.; Ong, S.P.; Moore, C.J.; Fischer, C.C.; Persson, K.A.; Ceder, G. Formation enthalpies by mixing GGA and GGA U calculations. *Phys. Rev. B Condens. Matter Mater. Phys.* **2011**, *84*, 045115. [[CrossRef](#)]
27. Dudarev, S.; Botton, G.; Savrasov, S.; Humphreys, C.; Sutton, A. Electron-energy-loss spectra and the structural stability of nickel oxide: An LSDA U study. *Phys. Rev. B Condens. Matter Mater. Phys.* **1998**, *57*, 1505–1509. [[CrossRef](#)]
28. Akimoto, J.; Gotoh, Y.; Oosawa, Y. Refinement of hexagonal BaTiO₃. *Acta Crystallogr. Sect. C* **1994**, *50*, 160. [[CrossRef](#)]
29. Yajima, T.; Kitada, A.; Kobayashi, Y.; Sakaguchi, T.; Bouilly, G.; Kasahara, S.; Terashima, T.; Takano, M.; Kageyama, H. Epitaxial Thin Films of ATiO_{3-x}H_x (A = Ba, Sr, Ca) with Metallic Conductivity. *J. Am. Chem. Soc.* **2012**, *134*, 8782–8785. [[CrossRef](#)]
30. Sinclair, D.; Skakle, J.S.; Morrison, F.; Smith, R.; Beales, T. Structure and electrical properties of oxygen-deficient hexagonal BaTiO₃. *J. Mater. Chem.* **1999**, *9*, 1327–1331. [[CrossRef](#)]
31. Takeiri, F.; Aidzu, K.; Yajima, T.; Matsui, T.; Yamamoto, T.; Kobayashi, Y.; Hester, J.; Kageyama, H. Promoted Hydride/Oxide Exchange in SrTiO₃ by Introduction of Anion Vacancy via Aliovalent Cation Substitution. *Inorg. Chem.* **2017**, *56*, 13035–13040. [[CrossRef](#)]
32. Ueda, Y.; Kobayashi, Y.; Itoh, M. Tailoring a new oxyhydride, CaVO_{3-x}H_x, with ordered hydride anions. *J. Solid State Chem.* **2022**, *305*, 122685. [[CrossRef](#)]
33. Mikita, R.; Aharen, T.; Yamamoto, T.; Takeiri, F.; Tang, Y.; Yoshimune, W.; Fujita, K.; Yoshida, S.; Tanaka, K.; Batuk, D.; et al. Topochemical Nitridation with Anion Vacancy-Assisted N³⁻/O²⁻ Exchange. *J. Am. Chem. Soc.* **2016**, *138*, 3211–3217. [[CrossRef](#)] [[PubMed](#)]

-
34. Miyazaki, M.; Ogasawara, K.; Nakao, T.; Sasase, M.; Kitana, M.; Hosono, H. Hexagonal $\text{BaTi}_{3-x}\text{H}_x$ Oxyhydride as a Water-Durable Catalyst Support for Chemoselective Hydrogenation. *J. Am. Chem. Soc.* **2022**, *144*, 6453–6464. [[CrossRef](#)] [[PubMed](#)]
 35. Tibshirani, R. Regression shrinkage and selection via the lasso. *J. R. Stat. Soc. Ser. B* **1996**, *58*, 267–288. [[CrossRef](#)]